Supplementary Materials for

Ångström-resolved Interfacial Structure in Buried Organic-Inorganic Junctions

Authors: Craig P. Schwartz[1*], Sumana L. Raj[2], Sasawat Jamnuch[3], Chris J. Hull[2,3], Paolo Miotti[4,5],Royce K. Lam[2,3], Dennis Nordlund[6], Can B. Uzundal[2], Chaitanya Das Pemmaraju[7], Riccardo Mincigrucci[8], Laura Foglia[8], Alberto Simoncig[8], Marcello Coreno[9], Claudio Masciovecchio[8], Luca Giannessi[8,10], Luca Poletto[4], Emiliano Principi[8], Michael Zuerch[2,11,12,13], Tod A. Pascal[3,14,15], Walter S. Drisdell[1,16*], Richard J. Saykally[1,3*]

Affiliations:

1. Chemical Sciences Division, Lawrence Berkeley National Laboratory, Berkeley, California 94720, USA
2. Department of Chemistry, University of California, Berkeley, California 94720, USA
3. ATLAS Materials Science Laboratory, Department of NanoEngineering and Chemical Engineering, University of California, San Diego, La Jolla, California, 92023, USA
4. Institute of Photonics and Nanotechnologies, National Research Council of Italy, via Trasea 7, I-35131 Padova, Italy
5. Department of Information Engineering, University of Padova, via Gradenigo 6/B, I-35131 Padova, Italy
6. Stanford Synchrotron Radiation Lightsource, SLAC National Accelerator Laboratory, Menlo Park, California 94025, USA
7. Theory Institute for Materials and Energy Spectroscopies, SLAC National Accelerator Laboratory, Menlo Park, California 94025, USA
8. Elettra-Sincrotrone Trieste S.C.p.A., Strada Statale 14–km 163.5, 34149 Trieste, Italy
9. ISM-CNR, Istituto di Struttura della Materia, LD2 Unit, Trieste, Italy
10. ENEA, C.R. Frascati, Via E. Fermi 45, 00044 Frascati (Rome), Italy
11. Materials Sciences Division, Lawrence Berkeley National Laboratory, Berkeley, California 94720, USA
12. Institute for Optics and Quantum Electronics, Abbe Center of Photonics, University of Jena, Jena, Germany
13. Fritz Haber Institute of the Max Planck Society, Berlin, Germany
14. Materials Science and Engineering, University of California San Diego, La Jolla, California, 92023, USA
15. Sustainable Power and Energy Center, University of California San Diego, La Jolla, California, 92023, USA
16. Joint Center for Artificial Photosynthesis, Lawrence Berkeley National Laboratory, Berkeley, California 94720, USA

*Correspondence to: *cpschwartz@lbl.gov (C.P.S.), *wsdrisdell@lbl.gov (W.S.D.), *saykally@berkeley.edu (R.J.S.)

This file includes:

Materials and Methods

Experimental Methods:

At the EIS-TIMEX endstation at FERMI, in order to access input photon energies from 184 to 195 eV, the 13th harmonic of FEL-1 and the 3rd harmonic of FEL-2 were used. The energy was tuned within this range by using the OPA to adjust the seed laser photon energies. Photon energies from 195 to 200 eV were accessed using the 10th harmonic of FEL-1 and the 4th harmonic of FEL-2. The FEL was focused to a ca. 10 μm diameter spot. Intensities necessary to generate signal were on the order of 10^{12} W/cm^2. In order to examine the SHG-SXR intensity as a function of input intensity, the latter was varied using different metallic filters before the sample (100 nm of Zr, 100 nm of Pd, and 200 nm of Pd), in addition to inherent pulse-to-pulse energy fluctuations of the FEL. Pulse energies were above the damage threshold for the samples, so samples were rastered after each shot such that every shot impacted a fresh spot on the samples. An iris was also used upstream of the sample to minimize the off-axis light from the FEL incident on the sample and detector. After the sample, the fundamental intensity was attenuated using 200 nm of aluminum before passing through a slit. The filter transmissions were calculated using the fundamental signal detected by the CCD when there was no sample in place. The exact photon energies of the FEL were also calculated using the position of the fundamental signal on the CCD. Both the fundamental and SHG signals were detected simultaneously using a soft X-ray spectrometer (2400 groove/mm grating) and CCD (Princeton Instruments PIXIS-XO 400B) [1].

Parylene-N has been previously well studied, including multiple X-ray studies as well as AFM, XPS and phase contrast imaging [2–4]. The molecular weight was estimated to be approximately 3 x 10^5. [5,6] Standard transmission values for aluminum, boron, and Parylene-N were used to account for the effects of the aluminum filter after the sample, and transmission through the sample itself. Only pulses with a single peak in the spectrum were used. The data were also filtered based on the full width at half maximum (FWHM) of the fundamental signal on the CCD to ensure that multiple overlapping modes were not present. Data taken with no sample in the X-ray beam were used to subtract the unwanted SHG signal generated in the FEL from the SHG signal generated at the sample.

Theoretical Methods:

First-principles density functional theory (DFT) [7,8] calculations were carried out using ***exciting*** [9] full potential all-electron software package which implements linearized augmented planewave methods. For simulations of B/V, two and three layers of icosahedral boron supercells were set up for SHG response calculations. The SHG response is nearly identical (Figure S8). A vacuum of 10 Å was added along the z-direction (perpendicular to the boron surface) to resample a boron-vacuum interface. The B/PN simulation was set up with one layer of icosahedral born and a single Parylene-N monomer (p-xylene). The B/E simulation was setup with two or three layers of ethane. Initially, an UFF forcefield [10] was used to optimize the structure. Next CP2K [11] was used to optimize the structure again to provide a more accurate geometry. For ground state simulation in ***exciting***, the parameter rgkmax was set to 7. This parameter represents the product between R_{MT}, the minimum muffin tin radius, and the maximum length of the **G+k** vector of the basis set. The Brillouin zone was sampled using 20x20x1 Γ-point centered k-point grid. The Perdew-Zunger Local Density Approximation (LDA-PW) [12] was used to model the exchange correlation effect within DFT. Core-hole 1s orbitals of boron were included in the

valance self-consistent field for Kohn-Sham eigenvalues and eigenvectors to self-consistently update in the simulations. The theoretical calculation of SHG followed the framework of established by Lam *et al* [13]. All spectral simulations were performed on geometry-optimized structures.

To calculate the SH response at B K-edge, we employed the formalism from Sharma [14] implemented within ***exciting***. The approach calculates the second-order susceptibility $\chi^{(2)}(2\omega, \omega, \omega)$ from the resonant energies at ω and 2ω excitation. We employed the independent particle approximation in which the excitation energy is given by the difference between their respective Kohn-Sham eigenvalues. The linear absorption spectra were calculated within the same formalism and a rigid 26 eV blue shift was applied to the spectra to match with the experimental results. The boron K edge is situated ~180 eV below the Fermi level, and so resonant excitation occurs when ω is at 188 eV (6.89 nm). To capture the contribution of B 1s excitation near 2ω, 2000 empty Kohn-Sham eigenstates whose energies extend up to ~225 eV above Fermi level were included in the calculation. The electronic density of state (DOS) hundreds of eV above the Fermi level exhibits slow convergence which leads to noisy response functions and impractical calculation of $\chi^{(2)}$ at high energies. Therefore, we added a heuristic imaginary part that is dependent on energy to account for lifetime broadening. Hence the energy expression becomes:

$$E_m \rightarrow E_m + i\Gamma(E_m) \; where \; \Gamma(E) = \frac{1}{\lambda}\sqrt{E - E_F}$$

Here λ is the inelastic free electron path which is ~8 Å in boron [15]. Lastly, the background signal from the valance electrons, which approximately decays as ~ $\frac{1}{Energy}$, was subtracted from output signal. The real and imaginary parts of the output signals were fit with the analytical equation:

$$S = \frac{A_1}{(Energy - A_2)^{A3}} \; with \; A_3 \sim 1$$

After background subtraction, the real and imaginary $\chi^{(2)}$ responses were obtained.

In general, SHG requires the breaking of inversion symmetry on the length scale of the incoming radiation [16]. As bulk boron possesses inversion symmetry, no second harmonic response should be observed. However, at the surface, the inversion symmetry is broken leading to SHG responses from interfaces. In simulations, the supercell slab system reacts spatially to the homogenous electric field at both the surfaces as the system always exhibits inversion symmetry due to its few-layer size. Consequently, this leads to overall attenuation of the SHG signal. Thus, in order to generate a more accurate SHG response from the simulation, only one surface is selected to actively contribute to the SHG. This is achieved by considering only the B 1s electrons of only the first (top) layer of the two icosahedron boron cells of the slab in the self-consistent field calculation. For the bottom layer, the B 1s electrons are not included hence the inversion symmetry is artificially broken and the interfacial SHG response is obtained. In the multiple component systems, the inversion symmetry does not exist in the supercell slab and the SHG response can be directly calculated without further manipulation. The energy axis of these simulations was calibrated using the same energy shift needed to align the linear absorption spectra with our experiments.

Supplementary Text

Experimental

A representative CCD image is shown in Figure S1 for the data taken with an input energy of 190 eV and the boron/Parylene-N (B/PN) sample. The total intensity of each signal is determined by summing the intensities of all the pixels in the region of interest (ROI). Baseline corrections were done by subtracting the intensity of a ROI adjacent to that of the signal from the signal intensity. A CCD image was collected for each laser pulse, along with data from PADReS, the laser pulse diagnostic system upstream of the sample. From PADReS we could obtain on a shot-to-shot basis the FEL spectrum of the fundamental as a function of photon energy and intensity. The drain current from a mirror upstream of the sample was also recorded as it is proportional to the pulse intensity and was treated as linear, with no systematic deviation seen between the two measurements. A sample dataset for a single photon energy is shown in Figure S2. The data were first filtered based on the energy spectrum of the pulse upstream of the sample from PADReS. If the spectrum was of more than a single mode, the laser pulse is excluded from further analysis. Similarly, the distribution of full width at half maximum (FWHM) of the fundamental signal on the CCD is examined and any outliers of the FWHM box plot are filtered. The data is then binned (Fig. S3), with bins of 400 μJ used at lower intensities and bins of 300 μJ used at higher intensities. The distribution of signals within each bin is also calculated and outliers that lie beyond the outer fence of the box plot are filtered. The binned data is fit with a power series and the fit of the fundamental data taken with no sample is used to calibrate the input pulse energy axis. The SXR-SHG signal from the FEL (i.e., the SHG signal seen in the no sample data sets) is subtracted from the SXR-SHG signal of the sample. The signal is now corrected for the transmission of the sample and the detector efficiency. The SXR-SHG signal is then plot against the input energy squared (Fig. S4). The slope of the linear fit of this data is proportional to $\left|\chi^{(2)}\right|^2$. To confirm that the dependence is truly quadratic, as should be the case for SHG, a plot of log(signal) vs. log(input energy) can be fit to a line (Fig. S5). A quadratic function will result in a log-log plot with a slope of 2. As can be seen in Figure S6, the datasets all have slopes close to 2 indicating SXR-SHG.

XAS was taken at Beamline 8-2 of the Stanford Synchrotron Radiation Lightsource by measuring the drain current. To maximize XAS signal, the samples were modified slightly from those used for SXR-SHG measurements. To measure XAS of the B/V interface, samples consisting of500nm of B supported on 300nm of Parylene-N and mounted on silicon were used. To measure XAS of the B/PN interface, a sandwich of 100 nm of Parylene-N on 300 nm of boron backed with 500 nm of Parylene-N and mounted on doped silicon was used. These are in contrast to free-standing films used in SXR-SHG. Auger electron yield measurements were also attempted due to the shorter escape depth (few nm) as compared to TEY (< 10 nm), but adequate signal to noise could not be achieved.

It is possible to work in a reflection geometry for SHG, however this has rigorous requirements on the sample. Typically, a very smooth and well-polished surface is used. So while such a technique is quite valuable, it would not be feasible with the samples used here. [17,18]

Theoretical

Investigation of origin of difference in SH response:

To investigate the shift to SHG, an ethane molecule is used to replace the parylene-N monomer. The methyl group closest to boron surface is kept exactly the same with the

boron/parylene case. We show that the SXR-SHG spectra of B/E have similar lineshapes and absorption energies to those of B/PN (Figure S7). Therefore, the close proximity interaction between the two systems remains the same. The SHG response shows very similar result which indicates that the response is surface sensitive to the environment (Figure S8). The ethane orientation was chosen parallel to the surface to minimize the size of the unit cell, and 2 layers of boron were used, showing minor differences from 3 layer calculations

Dipole correction for surface calculation:

The supercell approach employed in DFT calculations of asymmetric slabs can often lead to a net surface dipole density and artificial electrical fields [19]. To ensure that there was no dipole effect on the calculation, the electrostatic potential of the simulation cell was calculated. As can be seen in Figure S9, the electrostatic potential in the vacuum region is flat. Hence, the vacuum energy level can be established and no further dipole correction to the system is required. The electrostatic potential due to the presence of a dipole in the vertical direction was also calculated, but the result shows that the effect is negligible (see supporting information Figure S9), and so a dipole correction is not required. For the less computationally expensive B/V simulation, no significant difference is found between the SHG signal from two layers and three layers of boron.

Boron 1s core electronic states theoretical calculation:

The transition of 1s core electrons to the conduction band determines the energy required for X-ray absorption. Therefore, in order to verify the red shift observed at the B/PN and B/E interface, the density of states of B 1s electrons are calculated in Figure S10. The simulation is performed using ***exciting*** code at the independent particle approximation. The parameter ngrdos, which is the effective k-point mesh size, is set to 1000 and three point average smearing is used. The energy range in Hartree is -1 to 1 for the density of states around the fermi level (0 eV) and -6.4 to -6.25 for the 1s core. The calculation of DOS of 1s boron electron shows that there is an overall red shift to the core level electron in B/PN system, which is consistent with the calculated changes in the SHG spectra. Additionally, ground state calculations show that there is less charge in boron muffin-tin radius, which indicates that the presence of a coating weakens the surface boron bonds.

To further verify the origin of signal amplification, we calculated the projected DOS decomposed into 2s and 2p orbital contributions of the interfacial and bulk boron atoms (Fig. S11). We found that there is increased s-orbital character near the conduction band in the B/PN and B/E systems, which have better overlap with the excited 1s core electrons and therefore leads to an increase in the SHG intensity. Moreover, our calculations find that there are more of these s-like state at the Fermi level (0 eV) for the B/PN and B/E interfaces. Thus, screening due to the presence of an organic causes a redshift to the spectrum while the increase in the number of electronic states at the Fermi level leads to the amplification in SXR-SHG.

Computational Resources:

This research used resources at the National Energy Research Scientific Computing Center, a DOE Office of Science User Facility supported by the Office of Science of the U.S. Department of Energy, under allocation M696. A total of 1,200,000 supercomputing hours (SUs) were used in this work. One SU is equivalent to one processor working for one hour. Additional

computational simulations were performed at San Diego Supercomputer Center, under the Extreme Science and Engineering Discovery Environment (XSEDE), under allocation CSD626, using a total of 150,000 SUs.

References:

S[1] L. Poletto, F. Frassetto, P. Miotti, A. Di Cicco, P. Finetti, C. Grazioli, F. Iesari, A. Kivimäki, S. Stagira, and M. Coreno, *Spectrometer for X-Ray Emission Experiments at FERMI Free-Electron-Laser*, Review of Scientific Instruments **85**, 103112 (2014).

[2] G.-R. Yang, Y.-P. Zhao, J. M. Neirynck, S. P. Murarka, and R. J. Gutmann, *Chemical-Mechanical Polishing of Polymer Films: Comparison of Benzocyclobutene(BCB) and Parylene-N Films by XPS and AFM*, MRS Online Proceedings Library (OPL) **476**, (1997).

[3] M. A. Barstow, M. Lewis, and R. Petre, *Linear Absorption Coefficient of Beryllium in the 50–300-Å Wavelength Range*, J. Opt. Soc. Am., JOSA **73**, 1220 (1983).

[4] S. V. Gasilov, A. Ya. Faenov, T. A. Pikuz, I. Yu. Skobelev, F. Calegari, C. Vozzi, M. Nisoli, G. Sansone, G. Valentini, S. de Silvestri, and S. Stagira, *Phase-Contrast Imaging of Nanostructures by Soft x Rays from a Femtosecond-Laser Plasma*, Soviet Journal of Experimental and Theoretical Physics Letters **87**, 238 (2008).

[5] W. F. Beach, *A Model for the Vapor Deposition Polymerization of P-Xylylene*, Macromolecules **11**, 72 (1978).

[6] S. Ganguli, H. Agrawal, B. Wang, J. F. McDonald, T.-M. Lu, G.-R. Yang, and W. N. Gill, *Improved Growth and Thermal Stability of Parylene Films*, Journal of Vacuum Science & Technology A **15**, 3138 (1997).

[7] W. Kohn and L. J. Sham, *Self-Consistent Equations Including Exchange and Correlation Effects*, Phys. Rev. **140**, A1133 (1965).

[8] P. Hohenberg and W. Kohn, *Inhomogeneous Electron Gas*, Phys. Rev. **136**, B864 (1964).

[9] A. Gulans, S. Kontur, C. Meisenbichler, D. Nabok, P. Pavone, S. Rigamonti, S. Sagmeister, U. Werner, and C. Draxl, *Exciting: A Full-Potential All-Electron Package Implementing Density-Functional Theory and Many-Body Perturbation Theory*, J. Phys.: Condens. Matter **26**, 363202 (2014).

[10] A. K. Rappe, C. J. Casewit, K. S. Colwell, W. A. Goddard, and W. M. Skiff, *UFF, a Full Periodic Table Force Field for Molecular Mechanics and Molecular Dynamics Simulations*, J. Am. Chem. Soc. **114**, 10024 (1992).

[11] J. Hutter, M. Iannuzzi, F. Schiffmann, and J. VandeVondele, *Cp2k: Atomistic Simulations of Condensed Matter Systems.*, WIREs Comput Mol Sci **4**, 15 (2014).

[12] J. P. Perdew and A. Zunger, *Self-Interaction Correction to Density-Functional Approximations for Many-Electron Systems*, Phys. Rev. B **23**, 5048 (1981).

[13] R. K. Lam, S. L. Raj, T. A. Pascal, C. D. Pemmaraju, L. Foglia, A. Simoncig, N. Fabris, P. Miotti, C. J. Hull, A. M. Rizzuto, J. W. Smith, R. Mincigrucci, C. Masciovecchio, A. Gessini, E. Allaria, G. De Ninno, B. Diviacco, E. Roussel, S. Spampinati, G. Penco, S. Di Mitri, M. Trovò, M. Danailov, S. T. Christensen, D. Sokaras, T.-C. Weng, M. Coreno, L. Poletto, W. S. Drisdell, D. Prendergast, L. Giannessi, E. Principi, D. Nordlund, R. J. Saykally, and C. P. Schwartz, *Soft X-Ray Second Harmonic Generation as an Interfacial Probe*, Physical Review Letters **120**, (2018).

[14] S. Sharma and C. Ambrosch-Draxl, *Second-Harmonic Optical Response from First Principles*, Phys. Scr. **2004**, 128 (2004).

[15] P. Prieto, C. Quirós, E. Elizalde, and J. M. Sanz, *Electron Inelastic Mean Free Path and Dielectric Properties of A-Boron, a-Carbon, and Their Nitrides as Determined by Quantitative Analysis of Reflection Electron Energy Loss Spectroscopy*, Journal of Vacuum Science & Technology A: Vacuum, Surfaces, and Films **24**, 396 (2006).
[16] N. Bloembergen, R. K. Chang, S. S. Jha, and C. H. Lee, *Optical Second-Harmonic Generation in Reflection from Media with Inversion Symmetry*, Phys. Rev. **174**, 813 (1968).
[17] C. B. Uzundal, S. Jamnuch, E. Berger, C. Woodahl, P. Manset, Y. Hirata, T. Sumi, A. Amado, H. Akai, Y. Kubota, S. Owada, K. Tono, M. Yabashi, J. W. Freeland, C. P. Schwartz, W. S. Drisdell, I. Matsuda, T. A. Pascal, A. Zong, and M. Zuerch, *Polarization-Resolved Extreme Ultraviolet Second Harmonic Generation from LiNbO$_3$*, ArXiv:2104.01313 [Cond-Mat] (2021).
[18] E. Berger, S. Jamnuch, C. Uzundal, C. Woodahl, H. Padmanabhan, A. Amado, P. Manset, Y. Hirata, I. Matsuda, V. Gopalan, Y. Kubota, S. Owada, K. Tono, M. Yabashi, Y. Shi, C. Schwartz, W. Drisdell, J. Freeland, T. Pascal, and M. Zuerch, *Direct Observation of Symmetry-Breaking in a "ferroelectric" Polar Metal*, (2020).
[19] L. Bengtsson, *Dipole Correction for Surface Supercell Calculations*, Phys. Rev. B **59**, 12301 (1999).

Figures:

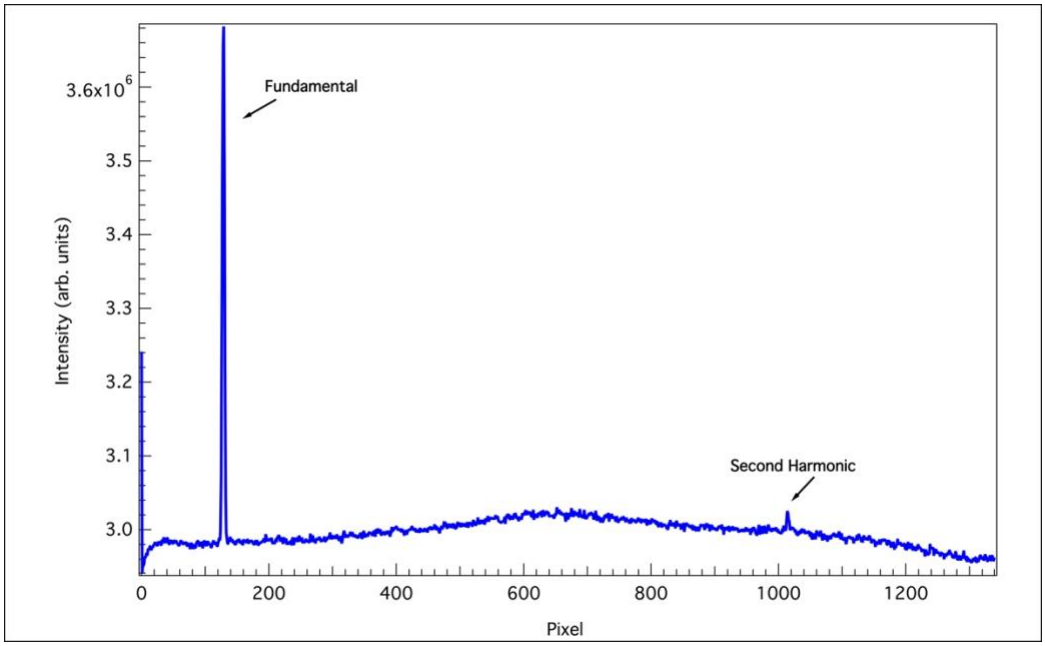

Figure S1: Representative CCD image projection shown for the sum of 20 laser shots on the boron sample. The fundamental was at 190 eV and is seen on the CCD at pixels 108 to 133. The SHG from both the sample and FEL source is seen at pixels 1002 to 1012 which corresponds to a photon energy of 386 eV. Baseline correction for the fundamental was performed using adjacent pixels (133 to 158) and the same was done for the SHG using pixels 1022 to 1042.

I)

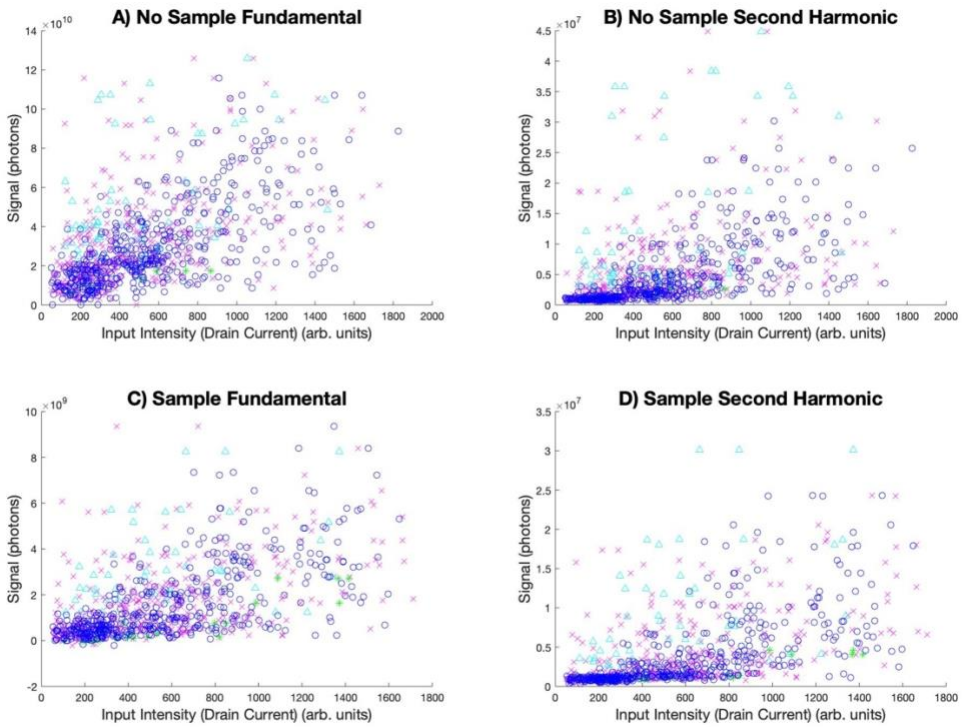
A) No Sample Fundamental
B) No Sample Second Harmonic
C) Sample Fundamental
D) Sample Second Harmonic
Signal (photons)
Input Intensity (Drain Current) (arb. units)

II)

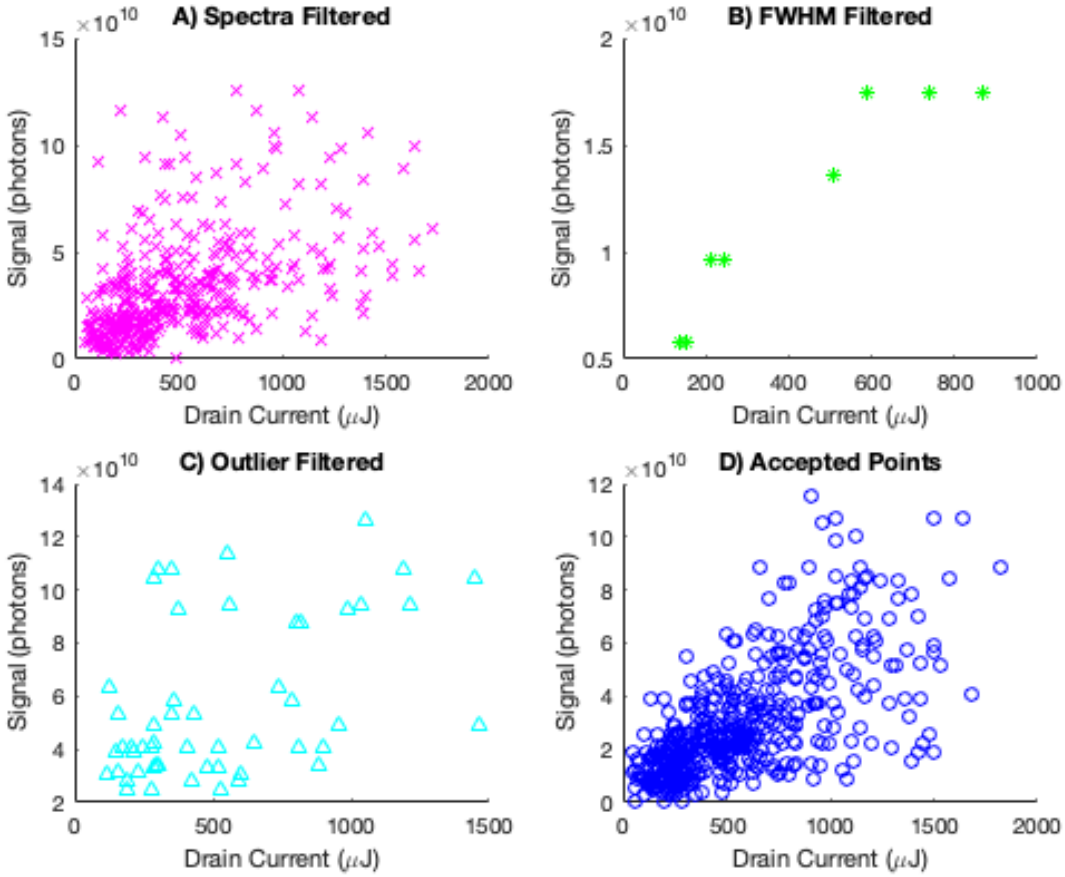

Figure S2: I) Plot of all laser shots vs. input drain current. Data taken at an input photon energy of 191 eV is shown in this plot. The total fundamental signal intensity (a) and total SHG signal intensity (b) with no sample are shown along with the fundamental (c) and SHG (d) signal intensities with the B/PN sample in place. Points were filtered and removed based on the pulse spectrum (x), fundamental signal FWHM (*), and bin outliers (Δ). Only the remaining points (o) are used in further calculations. The background second harmonic signal is estimated to be 0.03%. The deviation in this number between shots is minimized by strongly filtering the FEL based on the signal from the fundamental. II) Example of the filtering done in I part a). The removed points are shown separately, consisting of a) points removed based on the pulse spectrum (x), b) points removed based on the fundamental signal FWHM (*), c) points removed based on bin outliers (Δ) and d) the remaining signal points (o). The filtering methods remove roughly 40%, 2% and 5% of points respectively, leaving approximately 50% of the 796 points to be used in the analysis.

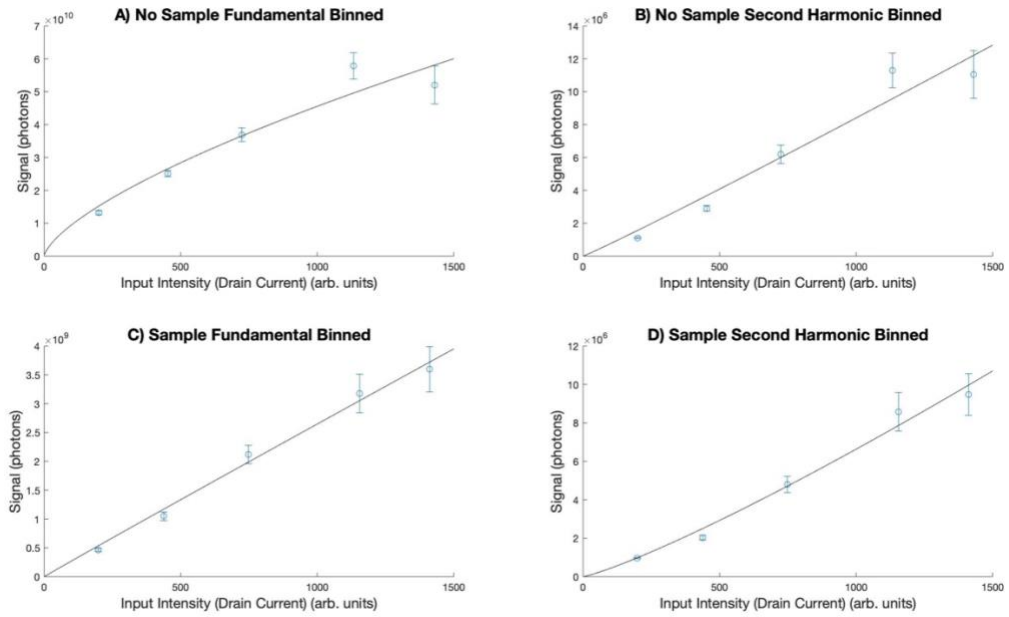

Figure S3: Binned and filtered signal vs. input drain current. The binned and filtered signals for the fundamental (a) and SHG (b) without a sample, and the fundamental (c) and SHG (d) with the B/PN sample are shown for an input energy of 191 eV. The contamination of the second harmonic contamination from the source is not completely linear with regards to the intensity of the fundamental.

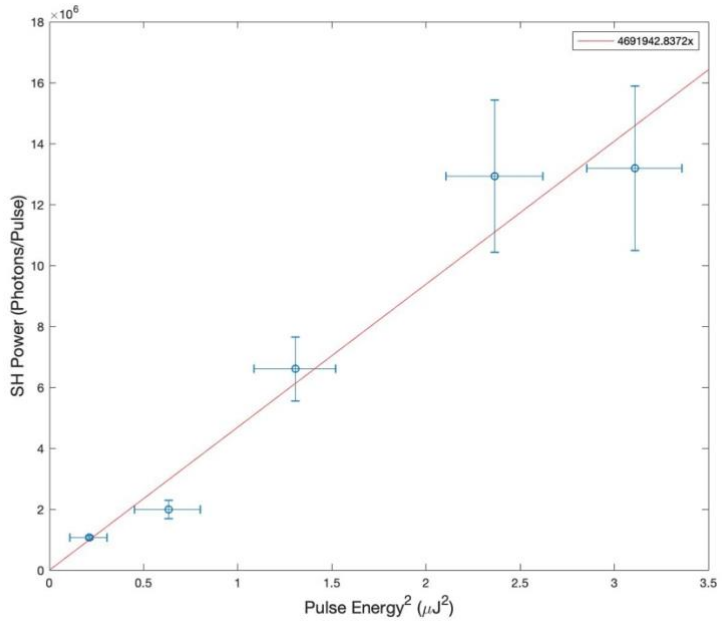

Figure S4: SHG generated by the sample vs. pulse energy squared. The SHG signal generated by the B/PN sample with an input photon energy of 191 eV is shown. The slope of the linear fit (4.6×10^6) is proportional to $|\chi^{(2)}|^2$. Fit R^2 is 0.952.

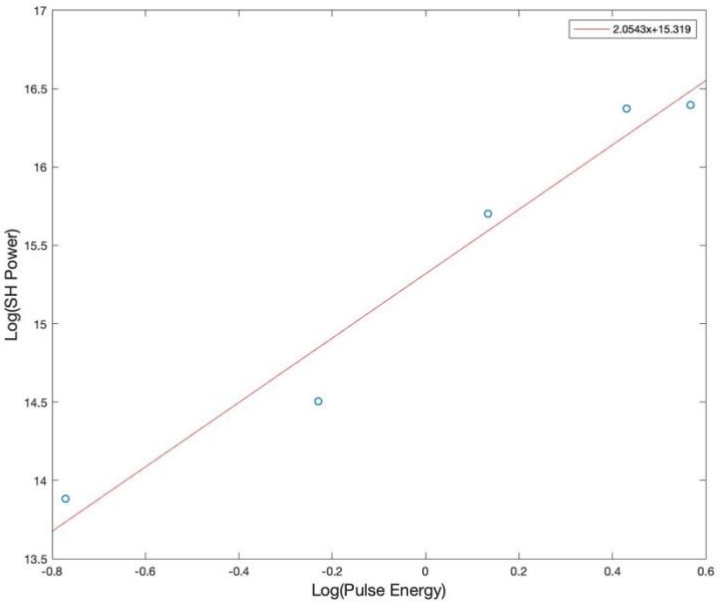

Figure S5: Representative log-log plot. The plot of log(SHG signal) vs. log(Pulse Energy) is fit with a line to confirm that the dependence is indeed quadratic. For a quadratic function the slope will be 2. Here, for the data taken at an input energy of 191 eV and with the B/PN sample, the slope is 2.0. Fit R^2 is 0.963.

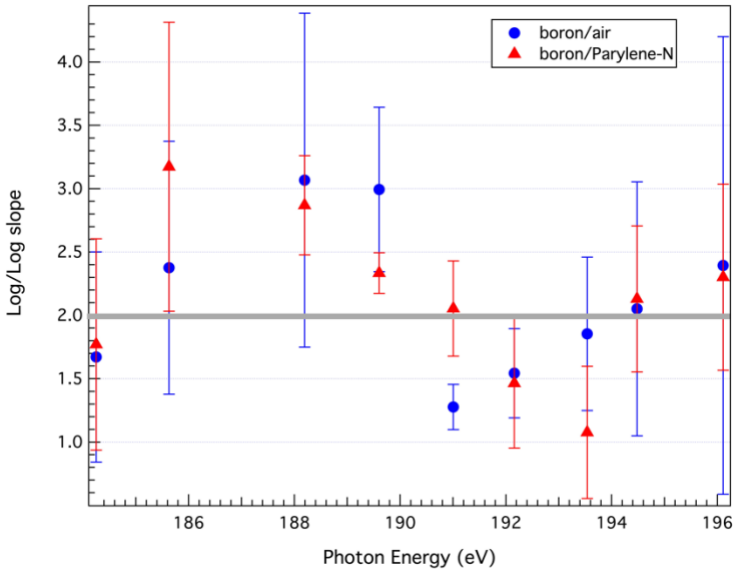

Figure S6: Log-log slopes for all datasets, B/V (blue) and B/PN (red). The log-log slopes are shown with their standard errors for all wavelengths and both samples, verifying that the signal we are seeing is in fact SXR-SHG. For a quadratic function, the log-log slope slope will be 2.

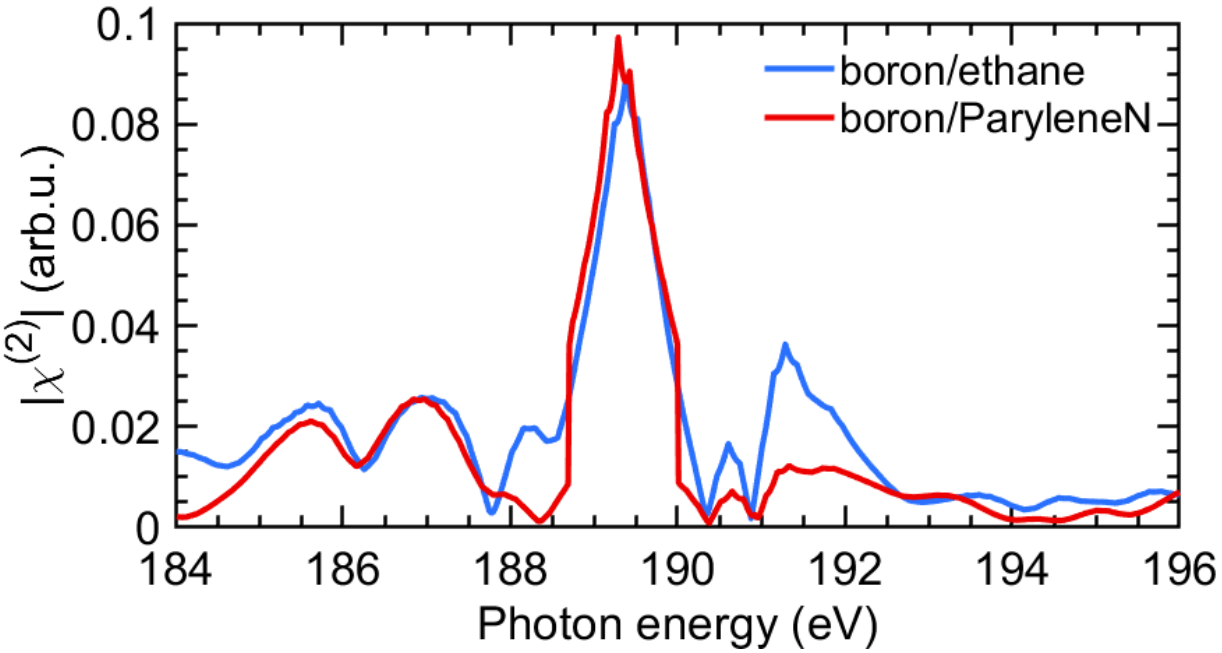

Figure S7: Calculated SXR-SHG spectral comparison between B/PN (blue) and B/E (orange) interface.

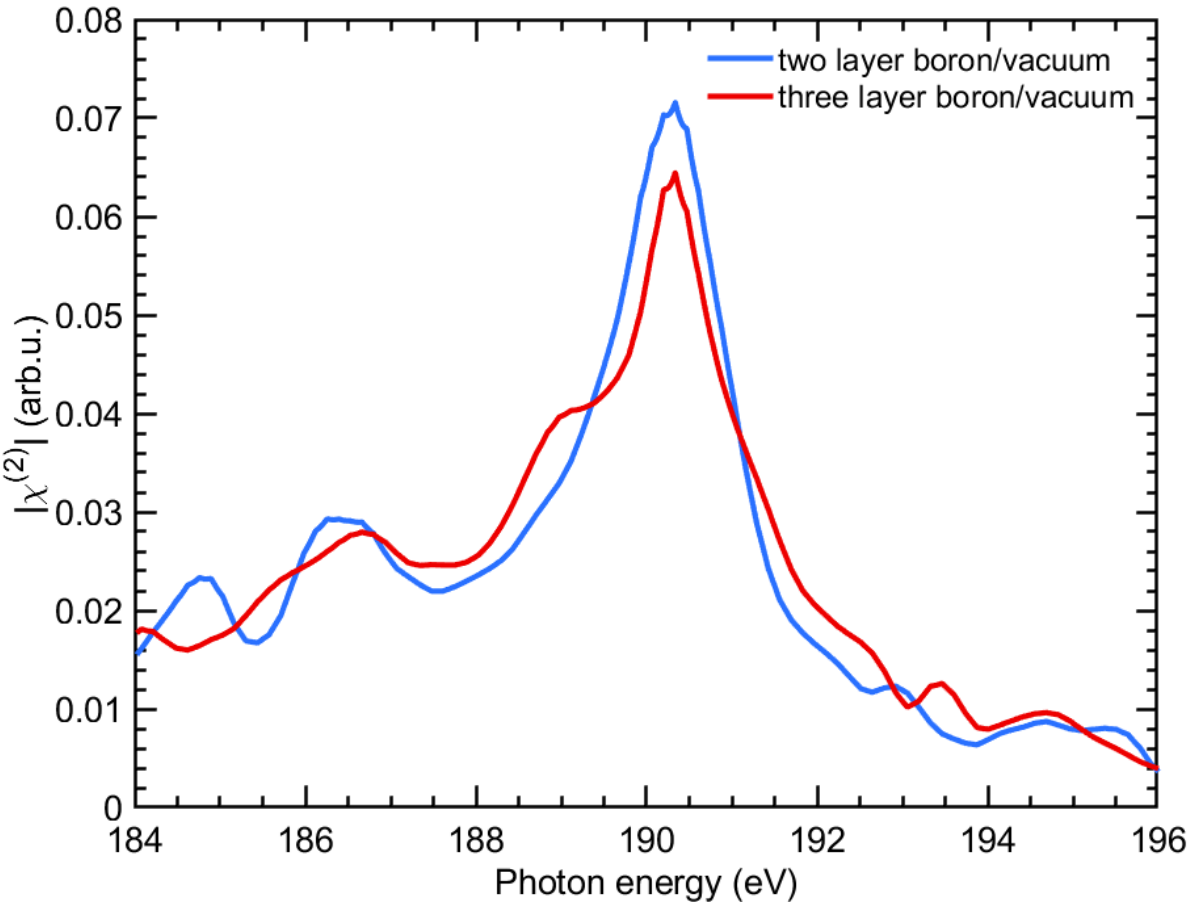

Figure S8: Calculated SXR-SHG spectra comparison between two layers (blue) and three layers (orange) of boron for the B/V interface.

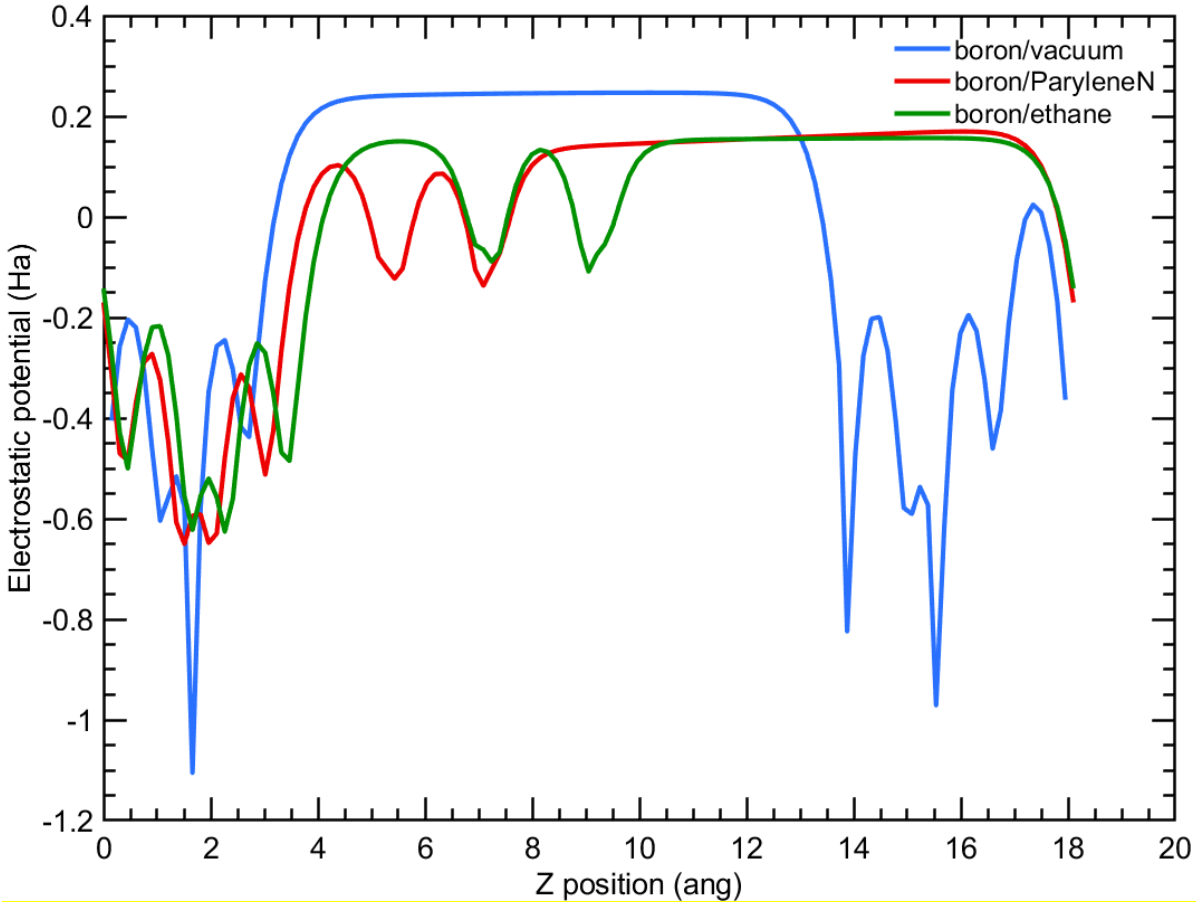

Figure S9: The calculated electrostatic potential at different z positions. The electrostatic potential as a function of position along the z axis (perpendicular to the slab) shows no dipole effect at the surface since the vacuum region (above ~3 Å) has a relatively constant potential. This is true for the B/V (blue), B/PN (orange) systems and B/E systems (yellow).

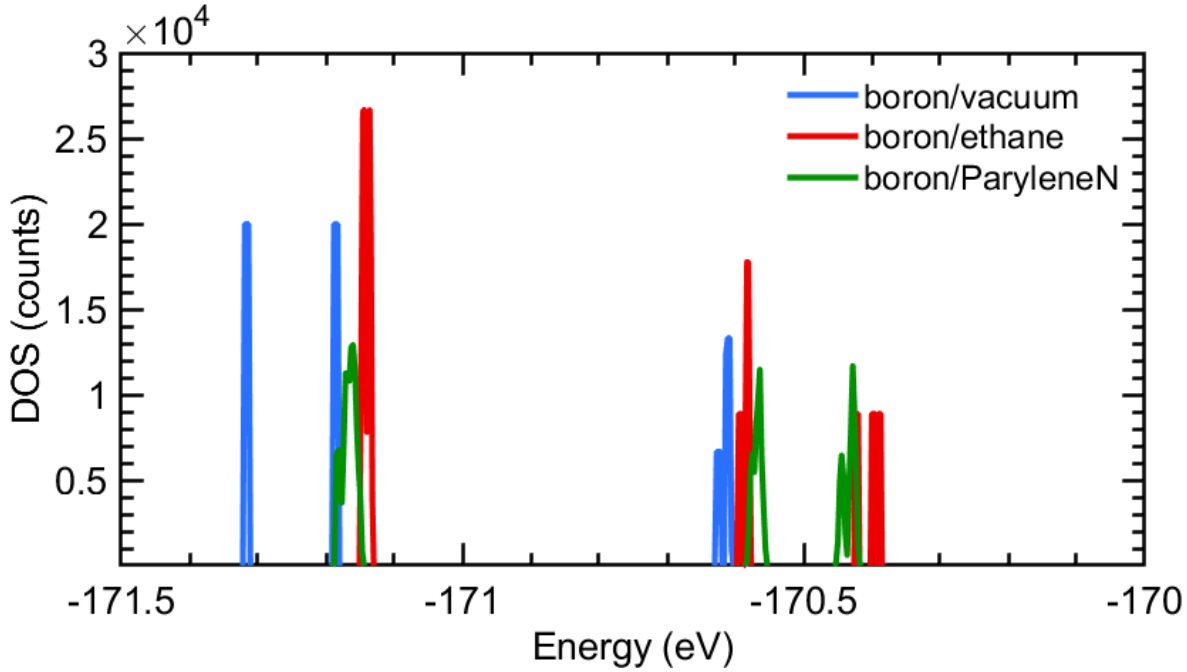

Figure S10: Calculated density of states for the interfaces studied here. The density of states of B/V (blue), B/PN(orange) and B/E (yellow) interfaces are shown.

a)

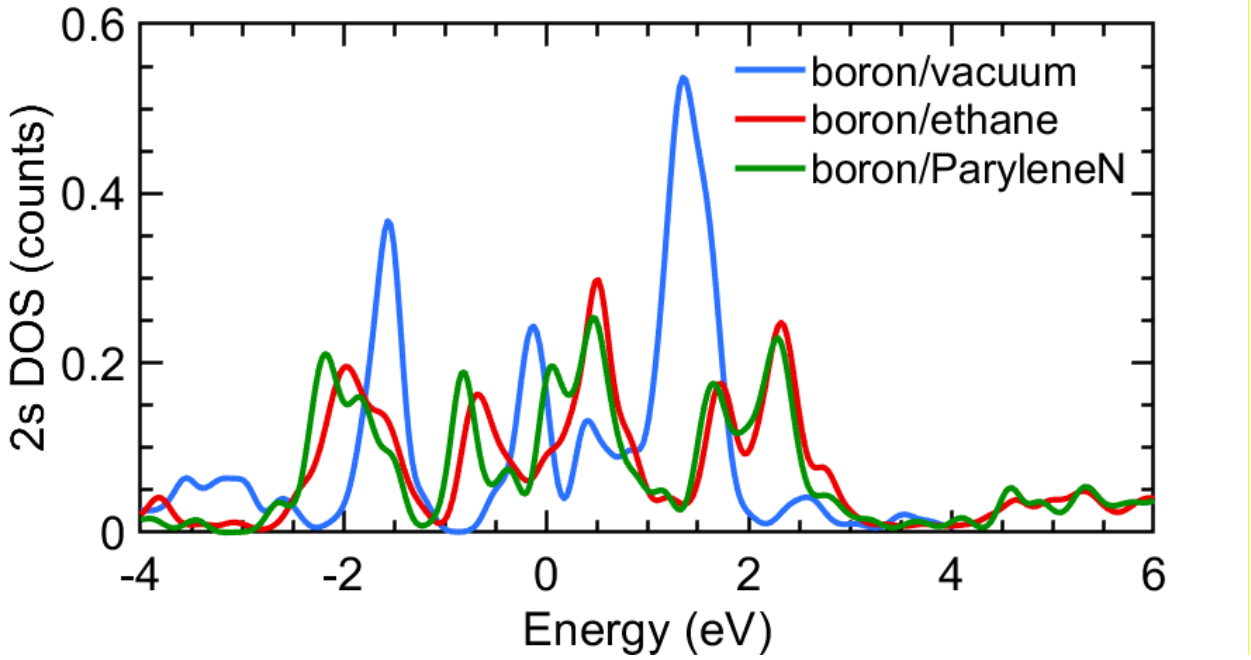

b)

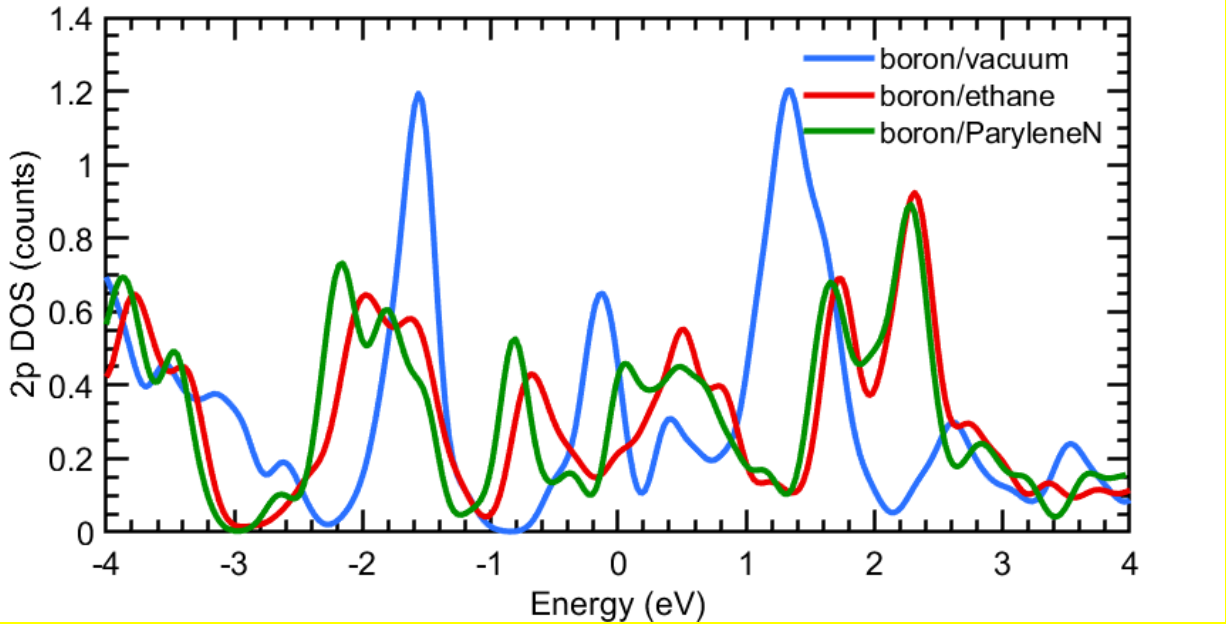

Figure S11: 2s and 2p contributions to the electronic density of states at the interface. The 2s orbital (a) and the 2p orbital (b) contributions to the electronic density of states at the interface are shown for the B/V (blue) B/PN (orange) and B/E (yellow) interfaces. There is more s-orbital character and more states near the Fermi level (0 eV) for the B/PN and B/E interface.